

# Efficient Bandwidth Estimation in Two-dimensional Filtered Backprojection PET Reconstruction

Ranjan Maitra

## Abstract

A method to efficiently estimate the bandwidth of the reconstruction filter in two-dimensional Positron Emission Tomography is presented. The approach uses matrix notation to recast the convolution Filtered Backprojection equation into its equivalent Backprojected Filtering form. Results on eigendecomposition of symmetric two-dimensional circulant matrices are derived and their computational implications in making reconstruction bandwidth estimation a simple extension of standard backprojected filtering investigated to provide a computationally efficient generalized cross-validation estimator. Performance evaluations on a wide range of simulation experiments are promising. The superior performance holds at both low and high total expected emissions, pointing to the method's applicability in a wide range of radio-tracer dosage situations. The approach is easily applied to the more general class of elliptically symmetric filters, with reconstruction performance often better than even that obtained with the true optimal radially symmetric filter.

## Index Terms

Backprojected filtering, circulant matrix, Emission Tomography Reconstruction, Filtered Backprojection, Gaussian kernel, Generalized Cross-Validation, Minimum Risk-Unbiased Estimation, Singular Value Decomposition

## I. INTRODUCTION

**F**ILTERED Backprojection (FBP) is the most commonly used reconstruction method in clinical two-dimensional (2D) Positron Emission Tomography (PET) imaging [1]–[4]. Even though other more sophisticated statistical methods [5]–[7] exist, FBP is preferred because of its computational speed and because most of the gains associated with these other methods typically occur in background regions and are easily recovered by a quick postprocessing of the reconstructed images [8], [9]. However, the FBP reconstruction filter involves a bandwidth or resolution size parameter, often specified in terms of its full-width-at-half-maximum (FWHM), that must ideally be optimally set to provide spatially consistent reconstructions. Similar to nonparametric function estimation in the statistics literature, the quality of reconstruction is evaluated by *e.g.* the widely-used squared error loss function [10]–[14],

Data-dependent unbiased risk estimation techniques [15], [16] – with practical modifications [17] to adjust for the extra-Poisson variation in corrected PET data – have been developed. The methodology is interpretable as a form of cross-validation (CV). Most practitioners however forego bandwidth selection schemes that involve additional steps independent of reconstruction, and instead use a fixed bandwidth or a visual approach that typically undersmooths reconstructions.

The use of CV [18], [19] and its rotationally invariant form – Generalized CV (GCV) [20] – for bandwidth selection is quite prevalent in nonparametric function estimation [21] and image deblurring or restoration [22]–[24]. For moderate sample sizes, CV-estimated bandwidth selectors are the best performing smoothing techniques for both linear ridge- and nonparametric regression [25]. For regularized image reconstructions, [26] and [23] provide optimal GCV bandwidths for the image deblurring problem where a degraded version of the true image, after convolving via a point-spread function (PSF) is observed. Such bandwidths usually perform well [26] (however, see [27] for examples of undersmoothing) but, as discussed in Section 4.1 of [22], are impractical to obtain in applications like PET that require indirect function estimation. However, in PET, the mean of the idealized count data along each LOR is specified by a discretized version of a linear integral operator (the Radon transform) of the true radio-tracer distribution along that line. Consequently, Section II of this paper shows that the singular value decomposition (SVD) of the reconstruction (in matrix notation) can actually be very readily obtained from results on symmetric one-dimensional (1D) and 2D circulant matrices, which are also derived here. The Predicted Residual Sums of Squares (PRESS) can then be very easily obtained in a similar spirit to [20] and practically minimized en route to FBP reconstruction to obtain the GCV-estimated bandwidth. The methodology is evaluated on simulated 2D phantom data in Section III. The implementation and results show that GCV selection and PET reconstruction can be carried out in less than a second, achieving an integrated squared error that is very close to the ideal. Moreover, our optimal reconstructions have the maximum relative benefits at lower rates of emissions. Further, the methodology can be used to select parameters of the wider class of elliptically symmetric 2D kernel smoothers. Postprocessing such as in [8] can remove negative artifacts to further improve reconstruction quality. The paper concludes with some discussion including areas that could benefit from extensions of our development.

R. Maitra is Professor in the Department of Statistics at Iowa State University, Ames, Iowa, USA. This research was supported, in part, by the National Science Foundation under its CAREER Grant No. DMS-0437555 and the National Institute of Biomedical Imaging and Bioengineering (NIBIB) of the National Institutes of Health under its Award No. R21EB016212. The content of this paper is solely the responsibility of the author and does not represent the official views of the NSF or the NIH.

Manuscript received March 20, 2018.

## II. THEORY AND METHODS

### A. Background and Preliminaries

Suppose that we have sinogram data after correcting for attenuation, randoms and scatter at each of  $n$  LORs and that we use FBP to reconstruct the underlying 2D source distribution in an imaging grid of  $p$  pixels. In convolution form, the  $i$ th FBP-reconstructed pixel value is

$$\hat{\lambda}_i^h = \sum_{\theta=1}^{\Theta} \sum_{r=1}^R e_h(x_i \cos \theta + y_i \sin \theta - r) y_{r\theta}, \quad (1)$$

for  $i = 1, 2, \dots, p$ . Here,  $\{y_{r\theta}\}$  is the corrected sinogram data along the LOR indexed by  $(r, \theta)$ ,  $e_h(\cdot)$  is the convolution filter with resolution filter size (FWHM)  $h$ . The sinogram has  $n = R\Theta$  LORs in (1). Further, we assume that  $n > p$ . The summation over  $r$  is a convolution and efficiently achieved by using a series of 1D discrete Fast Fourier Transforms (FFT) and linear interpolation while the summation over  $\theta$  is the slower backprojection step. The Fourier Slice Theorem shows that there is an equivalent form of FBP called Backprojected Filtering (BPF) where the backprojection step is applied first and is followed by 2D convolution in the imaging domain [28]. BPF reconstructions have an equivalent characterization [8] as a smoothed least-squares (LS) solution in matrix form as

$$\hat{\lambda} = \mathbf{S}_h(\mathbf{K}'\mathbf{K})^{-1}\mathbf{K}'\mathbf{y}, \quad (2)$$

where  $\mathbf{y}$  is the  $n$ -dimensional vector of corrected Poisson data in the sinogram domain,  $\mathbf{K}$  is a discretized version of the Radon transform and  $\mathbf{S}_h$  is a smoothing matrix with FWHM  $h$ . The application of  $\mathbf{K}'$  to  $\mathbf{y}$  is *backprojection* and the multiplication by  $(\mathbf{K}'\mathbf{K})^{-1}$  is filtering and can be done using FFTs because the matrix  $(\mathbf{K}'\mathbf{K})^{-1}$  is approximately 2D circulant. Moreover, if the smoothing matrix  $\mathbf{S}_h$  is also chosen to be 2D circulant, the operation of  $\mathbf{S}_h(\mathbf{K}'\mathbf{K})^{-1}$  can be applied in a single convolution step. Our focus in this paper is the estimation of the optimal reconstruction bandwidth  $h$ .

Leave-one-out CV (LOOCV) is often used to choose the optimal filter resolution size in density estimation [12], [29]. For FBP, a LOOCV strategy would involve removing the observed  $y_{r,\theta}$  for the  $j$ th LOR  $(r, \theta)$ , obtaining an estimate of the source distribution  $(\hat{\lambda}_{-(r,\theta)})$ , projecting it along the LOR and then comparing the projected (predicted) value with the (observed)  $y_{r,\theta}$  in terms of its squared error. (For notational simplicity, we henceforth use  $y_j$  to denote the observed data at the  $j$ th LOR indexed by  $y_{r,\theta}$ , and  $\hat{\lambda}_{-j} \equiv \hat{\lambda}_{-(r,\theta)}$  for the reconstruction obtained by deleting the observation from the  $j$ th LOR.) Specifically, LOOCV leads to the PRESS statistic

$$\sum_{j=1}^n [(\mathbf{K}\hat{\lambda}_{-j}^h)_j - y_j]^2, \quad (3)$$

where  $(\mathbf{K}\hat{\lambda}_{-j}^h)_j$  is the  $j$ th coordinate of the expected emissions predicted from the leave- $j$ th-LOR-out reconstruction and is  $\mathbf{k}'_j \hat{\lambda}_{-j}^h$  with  $\mathbf{k}'_j$  denoting the  $j$ th row of  $\mathbf{K}$ . Optimizing (3) over  $h$  involves multiple evaluations of (3), each of which requires  $n$  reconstructions/projections (one for each left-out LOR). Further, removing any LOR damages the circulant structure of  $\mathbf{K}'\mathbf{K}$  limiting the use of the FFT. Optimizing (3) over  $h$  is consequently computationally impractical, so we derive an (alternative) invariant version of (3) that reduces to as an easily computed function of  $h$ .

### B. An Invariant PRESS Statistic and GCV Estimation of $h$

To obtain a GCV estimate of  $h$ , we first state and prove our

**Theorem 1.** *Let  $\mathbf{U} = [\mathbf{U}_1 \mathbf{U}_2]$  be the  $n \times n$  orthogonal matrix of the left singular vectors of  $\mathbf{K}$ , with  $\mathbf{U}$  partitioned into matrices  $\mathbf{U}_1$  and  $\mathbf{U}_2$  with  $p$  and  $n - p$  columns, respectively. Also, let  $\mathbf{\Omega}_h$  be the diagonal matrix of the  $p$  eigenvalues of the circulant matrix  $\mathbf{S}_h$  and  $c(h) = \text{trace}(\mathbf{\Omega}_h)/(n - p)$ . The GCV estimate of  $h$  for estimators of the form (2) minimizes*

$$\zeta(h) = \{\mathbf{z}'_1(\mathbf{I}_p - \mathbf{\Omega}_h)^2\mathbf{z}_1 + [1 + c(h)]^2\mathbf{z}'_2\mathbf{z}_2\}, \quad (4)$$

where  $\mathbf{z} = \mathbf{U}'\mathbf{y}$ ,  $\mathbf{z}_1 = \mathbf{U}'_1\mathbf{y}$ ,  $\mathbf{z}_2 = \mathbf{U}'_2\mathbf{y}$ .

*Proof.* See Appendix A. □

The SVD of any  $n \times p$  ( $n > p$ ) matrix is generally expensive, requiring computations on the order of at least  $20p^3/3$  [30]. However, the complete SVD is unnecessary to calculate (4) and obtaining  $\mathbf{U}'_1\mathbf{y}$  with  $\mathbf{U}_1$  as in Theorem 1 is enough because  $\mathbf{z}'_2\mathbf{z}_2$  can be computed from the identity  $\mathbf{y}'\mathbf{y} = \mathbf{y}'\mathbf{U}\mathbf{U}'\mathbf{y} = \mathbf{y}'\mathbf{U}_1\mathbf{U}'_1\mathbf{y} + \mathbf{y}'\mathbf{U}_2\mathbf{U}'_2\mathbf{y} = \mathbf{z}'_1\mathbf{z}_1 + \mathbf{z}'_2\mathbf{z}_2$ . So we devise a practical way to obtain  $\mathbf{U}'_1\mathbf{y}$ . Note that  $\mathbf{U}'_1\mathbf{y} = \mathbf{D}_\bullet^{-1}\mathbf{V}'\mathbf{K}'\mathbf{y}$  where  $\mathbf{D}_\bullet$  is the diagonal matrix of the  $p$  eigenvalues of  $\mathbf{K}'\mathbf{K}$  and  $\mathbf{V}$  is the matrix of right singular vectors of  $\mathbf{K}$ . Also, backprojection  $\mathbf{K}'\mathbf{y}$  is a necessary step in BPF. Our objective now is to efficiently compute  $\mathbf{D}_\bullet$  and  $\mathbf{V}'\mathbf{x}$  for any vector  $\mathbf{x}$ . We next derive some results on the eigendecomposition of real symmetric circulant matrices.

1) *Spectral decomposition of circulant matrices:* Let  $\mathbf{C} = \text{circ}(c_0, c_1, \dots, c_{p-1})$  denote a circulant matrix having first row given by the vector  $\mathbf{c} = (c_0, c_1, \dots, c_{p-1})'$ . Further, let  $\gamma_{j,p} = (1, \omega_{j,p}, \omega_{j,p}^2, \dots, \omega_{j,p}^{p-1})'$  where  $\omega_{j,p}$  is the  $j$ th of the  $p$  complex roots of unity for  $j = 1, 2, \dots, p$ . Then [31] shows that  $d_j = \mathbf{c}'\gamma_{j,p}$  is the  $j$ th eigenvalue of  $\mathbf{C}$ , with corresponding eigenvector  $\gamma_{j,p}$ . Thus the eigenvalues of any circulant matrix can be speedily computed using FFTs and then scaling to equate the mean to  $c_0$ . Also, if  $\Gamma_p$  is the matrix with columns given by these eigenvectors, then  $\Gamma_p'\mathbf{x}$  is the forward Discrete Fourier Transform (DFT) of  $\mathbf{x}$  while  $\Gamma_p\mathbf{x}$  is the inverse DFT of  $\mathbf{x}$ . However, these vectors are not necessarily real-valued and not directly useful to us for finding  $\mathbf{V}$ . So we derive further reductions for symmetric circulant matrices.

**Theorem 2.** *Let  $\mathbf{C}$  be a  $p \times p$  symmetric circulant matrix. Then the eigenvalues of  $\mathbf{C}$  are all real and the spectral decomposition of  $\mathbf{C} = \mathbf{V}\mathbf{D}\mathbf{V}'$  where, for even  $p$ ,  $\mathbf{V} = [\mathbf{1}/\sqrt{I}; \mathbf{C}; \pm\mathbf{1}/\sqrt{I}; \mathbf{S}]$  with  $\mathbf{1} = (1, 1, \dots, 1)'$ ,  $\pm\mathbf{1} = (1, -1, 1, -1, \dots, 1, -1)'$ ,  $\mathbf{C}$  and  $\mathbf{S}$  are  $p \times (p/2 - 1)$ -matrices with  $(j, k)$ th element given by  $\sqrt{2/p} \cos(2\pi k(j-1)/p)$  and  $\sqrt{2/p} \sin(2\pi(p-k)(j-1)/p)$ , respectively. Further,  $\mathbf{D}$  is the diagonal matrix of eigenvalues with  $k$ th eigenvalue*

$$d_k = c_0 + \sum_{j=1}^{p/2-1} c_j \cos\left(\frac{2\pi k j}{I}\right) + c_{p/2}(-1)^k; \quad 0 \leq k \leq p-1. \quad (5)$$

For odd  $p$ , the expression for the eigenvalues is the same but the last term is omitted. Also then,  $\mathbf{V}$  does not contain the column vector  $\pm\mathbf{1}$  and  $\mathbf{C}$  and  $\mathbf{S}$  are  $p \times (p-1)/2$ -matrices.

*Proof.* See Appendix B.  $\square$

**Corollary 3.** *For a real vector  $\mathbf{x} = (x_1, x_2, \dots, x_p)'$ , we have*

- 1)  $\alpha \doteq \mathbf{V}'\mathbf{x}$  can be computed directly from  $\beta \doteq \Gamma'\mathbf{x}$  by noting that the first and  $(p/2)$ th (for  $p$  even) elements of  $\alpha$  are the real parts of the corresponding elements of  $\beta$ . For  $k = 2, 3, \dots, [(p-1)/2]$ , the  $k$ th element of  $\alpha$  is the real part of the scaled sum of the  $k$ th and the  $(p-k+2)$ th elements of  $\beta$  while the  $(p-k+2)$ th element of  $\alpha$  is the imaginary part of the scaled difference of the  $k$ th and the  $(p-k+2)$ th elements of  $\beta$ . In both cases, the scaling factor is  $\sqrt{2}$ . Also, here  $[\xi]$  is the smallest integer less than or equal to  $\xi$ .
- 2) Let  $\psi_1 = (\sqrt{2}x_1, x_2, x_3, \dots, \sqrt{2}^{I[p \text{ even}]} x_{[p/2]+1}, \mathbf{0})'$ , where  $\mathbf{0}$  is a vector of 0's and  $I[\cdot]$  is the indicator function. Also, let  $\psi_2 = (\mathbf{0}, x_{[p/2]+2}, x_{[p/2]+3}, \dots, x_p)'$ . Then each element of  $\mathbf{V}\mathbf{x}$  is the sum of the real and imaginary parts of the corresponding elements of  $\Gamma'\psi_1/\sqrt{2}$  and  $\Gamma'\psi_2/\sqrt{2}$ , respectively.

*Proof.* Part 1 follows from the proof of Theorem 2 while part 2 follows by direct substitution.  $\square$

Corollary 3 means that both  $\mathbf{V}'\mathbf{x}$  and  $\mathbf{V}\mathbf{x}$  can be efficiently computed using FFTs. We now provide additional reductions on 2D circulant matrices needed to calculate (4) for BPF.

## 2) Spectral Decomposition of 2D Circulant Matrices:

**Definition 4.** *A 2D circulant matrix or, alternatively, a block-circulant-circulant-block (BCCB) matrix is a  $pq \times pq$ -dimensional matrix  $\mathbf{C}$  with  $p$  circulant blocks of  $q$ -dimensional circulant matrices. Thus,  $\mathbf{C} = \text{circ}(\mathbf{C}^{(0)}, \mathbf{C}^{(1)}, \dots, \mathbf{C}^{(p-1)})$ , where each  $\mathbf{C}^{(i)} = \text{circ}(c_0^{(i)}, c_1^{(i)}, \dots, c_{q-1}^{(i)})$ .*

Note that a symmetric BCCB matrix necessarily has symmetric blocks of symmetric circulant matrices. We now state a result on the eigen-decomposition of such matrices.

**Theorem 5.** *Let  $\{\gamma_{k,p}; k = 1, 2, \dots, p\}$  and  $\{\gamma_{k,q}; k = 1, 2, \dots, q\}$  be as in Section II-B1. The  $(k, j)$ th eigenvalue of a BCCB matrix  $\mathbf{C}$  is  $d_{k,j} = \sum_{l=0}^{p-1} \sum_{m=0}^{q-1} c_m^{(l)} \omega_{k,p}^l \omega_{j,q}^m$  and has eigenvector  $\gamma_{k,p} \otimes \gamma_{j,q}$ . Then the spectral decomposition of  $\mathbf{C} = (\Gamma_p \otimes \Gamma_q)\mathbf{D}(\Gamma_p \otimes \Gamma_q)'$  where  $\mathbf{D}$  is the diagonal matrix of eigenvalues  $\{d_{k,j}; j = 1, 2, \dots, q, k = 1, 2, \dots, p\}$ .*

*Proof.* The result follows by direct substitution and using the fact that  $\gamma_{k,p}$  and  $\gamma_{k,q}$  are eigenvectors of  $p \times p$  and  $q \times q$  1D circulant matrices, respectively.  $\square$

Theorem 5 means that 2D FFTs can be used for eigendecomposition of a BCCB matrix  $\mathbf{C}$ . More pertinently, the eigenvalues  $d_{k,j}$  are scaled versions of the 2D FFT of  $\mathbf{C}$ , with scaling factor that equates the mean  $d_{k,j}$  to the first element of  $\mathbf{C}$ . We now derive results for symmetric BCCB matrices.

**Corollary 6.** *Let  $\mathbf{V}_p$  and  $\mathbf{V}_q$  be as in Theorem 2. Then the spectral decomposition of a symmetric BCCB matrix  $\mathbf{C}$  is given by  $\mathbf{C} = (\mathbf{V}_p \otimes \mathbf{V}_q)\mathbf{D}(\mathbf{V}_p \otimes \mathbf{V}_q)'$ , with  $\mathbf{D}$  as in Theorem 5.*

*Proof.* Such a real spectral decomposition is guaranteed to exist by standard results on real symmetric matrices. Replacing  $\Gamma_p$  by  $\mathbf{V}_p$  and  $\Gamma_q$  by  $\mathbf{V}_q$  in Theorem 5 yields the result.  $\square$

Corollary 6 means that for BCCB matrices,  $\mathbf{V}'\mathbf{x}$  can be readily computed for any  $\mathbf{x}$  using forward FFTs. Hence,  $\mathbf{U}'_1\mathbf{y}$  of Theorem 1 can be easily calculated. Further, this is a one-time calculation that can be used in conjunction with the bandwidth-dependent parts of (4) to find the minimum. These latter calculations all involve linear operations on the FFT results and can be speedily executed.

### C. Extension to Elliptically Symmetric Smoothing Kernels

Most 2D FBP/BPF and PET reconstruction filters are radially symmetric. However, the wider general class of elliptically symmetric kernels (that may be radially asymmetric) such as the 2D Gaussian kernel with parameters  $(h_1, h_2, \rho)$

$$S_{h_1, h_2, \rho}(k, j) \propto \exp \left\{ -\frac{1}{1-\rho^2} \left( \frac{k^2}{h_1^2} + \frac{j^2}{h_2^2} - 2\rho \frac{kj}{h_1 h_2} \right) \right\} \quad (6)$$

provide greater flexibility because they may better account for more smoothness along particular directions provided by the natural orientation of elongated structures. However, visually selecting smoothing parameters for such kernels can be taxing because of the larger set of parameters involved. Also, FBP is difficult to implement with such kernels because it uses 1D filtering. However BPF uses 2D filtering and such kernels are straightforward to incorporate here: indeed, our calculations and derivations of Section II-B extend immediately, with  $h$  in (4) replaced by  $h_1, h_2, \rho$  and found using optimization methods such as in [32]. Thus, the developments in Section II-B make possible the use of the wider class of elliptically symmetric smoothing kernels in PET.

## III. PERFORMANCE EVALUATIONS

### A. Experimental Setup

The performance of our GCV approach was explored in a series of simulated but realistic 2D PET experiments. Our setup used the specifications and the sixth slice of the digitized Hofmann phantom (Figure 1a) in [33]. Our imaging domain was discretized into  $128 \times 128$  pixels of dimension 2.1 mm each, while our sinogram domain had  $128 \times 320$  distance-angle bins (LORs) of size  $2.1\text{mm} \times \pi/320$  radians. Pseudo-random Poisson realizations were simulated in the sinogram domain with

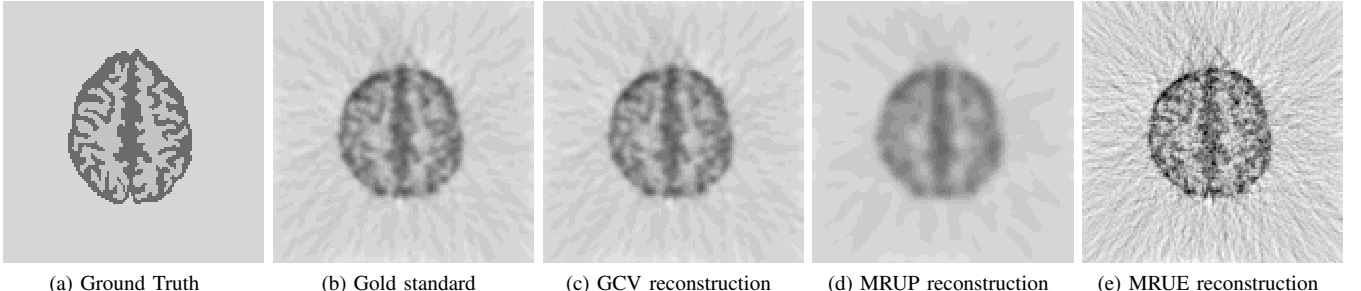


Fig. 1: (a) The phantom. BPF reconstruction using the (b) optimal, (c) GCV- (d) MRUE- and (e) MRUP-selected bandwidths.

mean intensity given by the corresponding discretized Radon transform of the phantom. The total expected counts  $\Lambda$  varied over 9 distinct equi-spaced (on a  $\log_2$  scale) values between  $\Lambda = 10^4$  and  $\Lambda = 10^6$  counts. Therefore,  $\Lambda$  ranged from the very low (about 0.61 counts per pixel) to the moderately high (61 counts per pixel) and matched the range of values typically seen in individual scans in dynamic 2D PET studies [34]. Our first set of evaluations used a radially symmetric Gaussian kernel  $S_h$  with FWHM  $h$  and were followed with experiments that used elliptically symmetric Gaussian kernels with parameters  $h_1, h_2, \rho$ . We use “BPFe” to denote BPF reconstructions with elliptically symmetric kernels and “GCVe” to denote GCV estimated parameters in these settings. We also evaluated performance in applying reducing negative artifacts as per of [8] – we add “+” in the nomenclature to denote this additional postprocessing step. For each simulated sinogram dataset, we obtained the optimal BPF, BPFe, BPFe+ and BPFe+ reconstructions and the corresponding optimal bandwidths as follows: for the BPF reconstruction  $\hat{\lambda}^h$  using a radially symmetric Gaussian filter with FWHM  $h$ , we calculated the Root Mean Squared Error (RMSE)  $\mathcal{R}_h = \|\hat{\lambda}^h - \lambda\| / \sqrt{p}$ , with  $\lambda$  the true source distribution (the Hoffman [33] phantom). The  $h_O$  corresponding to the BPF reconstruction that minimizes the RMSE (*i.e.*, the  $h_O$  such that  $\mathcal{R}_{h_O} \leq \mathcal{R}_h$  for all  $h \neq h_O$ ) is our *true optimal* FWHM for the simulated sinogram dataset. Similar optimal FWHM parameters and gold standard reconstructions are obtained for BPFe, BPFe+ and BPFe+ reconstructions (note that BPFe and BPFe+ have trivariate smoothing parameters.) We evaluated performance of reconstructions obtained using our GCV-estimated procedure ( $h_G$ ) in terms of the RMSE and compared them (for BPF and BPFe+ reconstructions) with corresponding calculations obtained using the minimum risk unbiased estimated [16], [17] bandwidths  $h_P$  and  $h_E$  obtained in the prediction (MRUP) and estimation (MRUE) domains respectively. We also evaluated performance of each reconstruction in terms of its RMSE efficiency relative to the gold standard reconstruction obtained using

$h_O$ , that is, we calculated RMSE efficiency for a BPFe reconstruction with filter resolution  $h$  as  $\mathcal{R}_h/\mathcal{R}_{h_O}$ . Similar evaluations were done for BPFe, BPFe+ and BPFe+ reconstructions, with the BPFe and BPFe+ bandwidth parameter sets also trivariate. Reducing negativity artifacts does not involve choosing a FWHM beyond that chosen for BPFe; however the optimal BPFe+ or BPFe+ bandwidths may be different from the corresponding optimal BPFe and BPFe bandwidths. We obtained 1000 simulated sinogram datasets and evaluated reconstruction performance using the different methods.

## B. Results

1) *Illustrative Examples:* We first illustrate performance on a sample simulated sinogram realization with  $\Lambda = 10^5$ .

a) *BPFe reconstruction:* Figure 1b provides the “gold standard” BPFe/FBP reconstruction obtained using  $h_O$ . BPFe

TABLE I: Bandwidths and RMSEs obtained with BPFe reconstructions and different bandwidth selection methods.

Estimation Method	Gold Standard	GCV	MRUP	MRUE
Optimal Bandwidth	3.183	3.279	15.32	1.397
RMSE ( $\times 10^{-5}$ )	8.376	8.378	10.32	10.83

reconstructions obtained using  $h_G$ ,  $h_P$  and  $h_E$  are in Figures 1c, 1d and 1e, respectively. Table I provides the estimated bandwidths and numerically summarizes performance in terms of the RMSEs. Performance using MRU bandwidth selection is not very satisfactory, with MRUE ( $h_E = 1.397$  pixels, RMSE =  $1.083 \times 10^{-4}$ ) and MRUP ( $h_P = 15.322$  pixels, RMSE =  $1.032 \times 10^{-4}$ ) considerably under- and over-estimating the bandwidths, respectively. (Following [16],  $h_P$  is specified in the 1D filtering domain of the projection distances, and is not directly comparable in numerical value to the 2D filter bandwidth). On the other hand, GCV ( $h_G = 3.279$  pixels, RMSE =  $8.378 \times 10^{-5}$ ) tracks the optimal value ( $h_O = 3.183$  pixels, RMSE =  $8.376 \times 10^{-5}$ ) very closely, both in terms of bandwidth selection and reconstruction ability.

b) *BPFe reconstruction:* Our next set of illustrations explored GCVe’s performance in choosing smoothing parameters for BPFe reconstructions. Figure 2 shows reconstructions obtained using the *true optimal* and the GCVe-selected parameters.

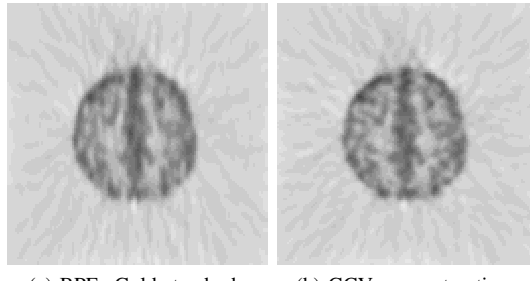


Fig. 2: BPFe reconstructions with the (a) optimal and (b) GCVe-estimated smoothing parameters.

The reconstruction RMSE (Table II) of  $8.367 \times 10^{-5}$  obtained using BPFe with GCVe even marginally outperforms BPFe

TABLE II: Summary of BPFe reconstruction performance.

Estimation Method	Optimal Parameters ( $h_1, h_2, \rho$ )	RMSE ( $\times 10^{-5}$ )
Gold Standard	(5.143, 2.488, -0.122)	8.289
GCVe-estimated	(3.249, 3.058, 0.170)	8.378

performance obtained using  $h_O$  while comparing favorably with the true optimal RMSE of  $8.289 \times 10^{-5}$ . The illustration shows some undersmoothing with GCVe and scope for improved parameter estimates, but our approach opens the possibility for further improvements to reconstruction by allowing for a wider class of reconstruction filters.

c) *Reconstructions with reduced negative artifacts:* Our final set of illustrations explores performance in BPFe+ and BPFe+ reconstructions, having gold standards as per Figure 3a ( $h_{O+} = 2.766$ ; RMSE =  $7.873 \times 10^{-5}$ ) and Figure 3d ( $h_1 = 3.818, h_2 = 2.216, \rho = -0.035$ ; RMSE =  $7.831 \times 10^{-5}$ ), respectively. For BPFe+, the GCV-estimated bandwidth of  $h = 3.279$  yields the reconstruction of Figure 3b with a RMSE of  $7.976 \times 10^{-5}$  while MRUP provides the BPFe+ reconstruction of Figure 3c with RMSE =  $1.008 \times 10^{-4}$ . For brevity of display, we forego discussing BPFe+ reconstructions done with MRUE-selected bandwidths, noting simply that they also improve over BPFe under BPFe+ (with RMSE =  $8.646 \times 10^{-5}$  in this example) but that improvement falls far short of that obtained using GCV. Figure 3e also shows improvement of BPFe+ over BPFe (RMSE =  $7.968 \times 10^{-5}$ ) when negative artifacts are eliminated using [8], but the improvement of BPFe+ over BPFe is very marginal. One aspect of note is that [8] reduces negative artifacts using a radially symmetric filter – an alternative approach that allows for greater flexibility in smoothing out negative values may be more appropriate.

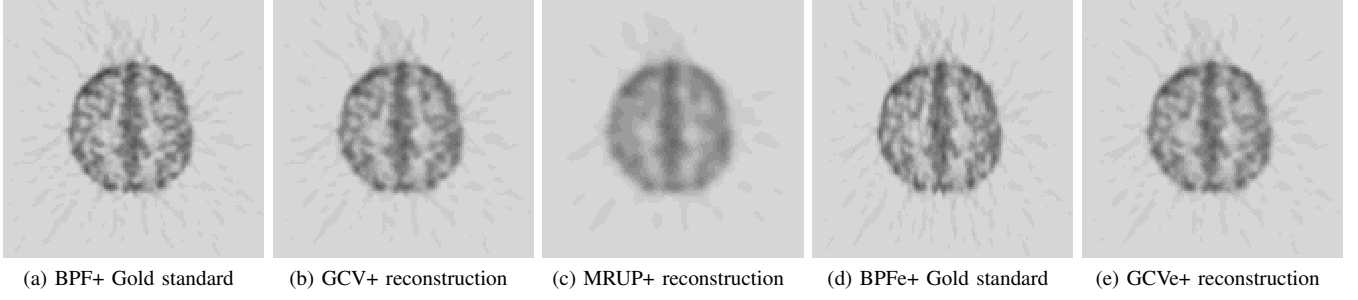


Fig. 3: (a-c) BPF+ reconstructions using the (a) optimal, (b) GCV- and (c) MRUP-estimated bandwidths. (d, e) BPFe+ reconstructions using the (d) optimal and (e) GCVe-estimated parameters.

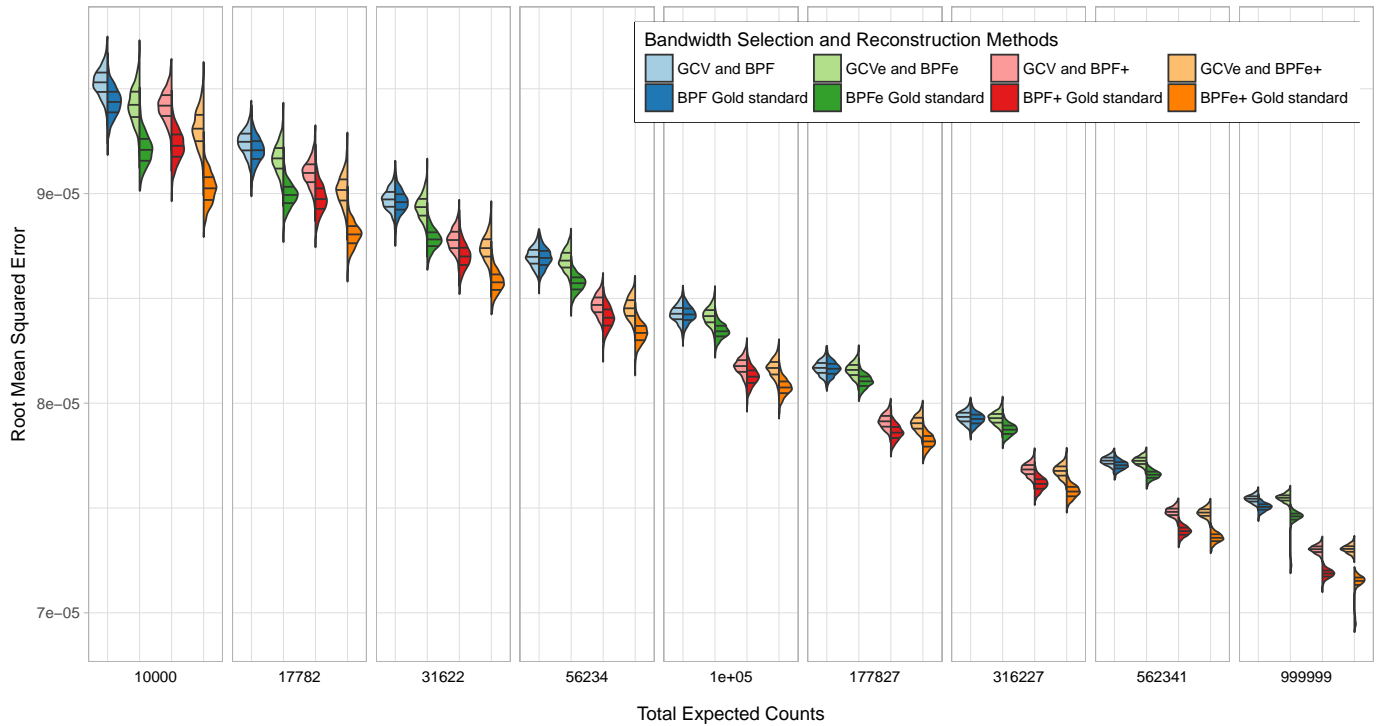


Fig. 4: Split violin plot distributions against total expected counts ( $\Lambda$ ) of the 1000 RMSEs for reconstructions using GCV-estimated (left lobe of the violin) and the corresponding gold standard (right lobe) reconstruction. At each  $\Lambda$ -value, violins are in the order of BPF, BPFe, BPF+ and BPFe+ reconstructions. The upper, median and lower quartiles are also displayed in that order on each split violin by means of bars.

2) *Large-scale Simulation Study*: We now report results of our large-scale simulation study on the performance (in terms of RMSE) of the different bandwidth selection and reconstruction methods and their distribution for different values of  $\Lambda$ . Reconstructions using MRU bandwidths have RMSEs substantially higher than those using the optimal or GCV-estimated bandwidths (Figure 4) and certainly for lower values of  $\Lambda$ , so we display performance of these estimators separately in Figure 5 in order to attain finer granularity for displays involving our methods. Figure 4 displays RMSEs of BPF, BPFe, BPF+ and BPFe+ reconstructions obtained with GCV and the corresponding true optimal bandwidth parameters. The RMSEs reported in this figure are much lower than those reported in Figure 5, and especially so for lower values of  $\Lambda$ . Also, BPFe reconstructions using the GCVe-estimated bandwidths have similar, if not lower RMSEs, to those obtained with the gold standard BPF reconstructions. Reducing negative artifacts as per [8] improves the quality of BPF or BPFe reconstructions that is more substantial at higher  $\Lambda$ -values. On the other hand, the improvement with using GCVe-estimated elliptically symmetric filters over GCV-estimated radially symmetric filters tapers off at higher total expected counts. However, the optimal BPFe estimator improves reconstruction quality in terms of having lower RMSEs over the gold standard BPF reconstructions. Thus, we see that the performance of GCVe-estimated reconstruction relative to the gold standard BPFe is not as strong as that of the GCV-estimated reconstruction relative to the BPF gold standard. This observation is also supported by the relative RMSE efficiency displays in Figure 6. This may be because, as per Table II of our illustrative example, the bandwidth parameter

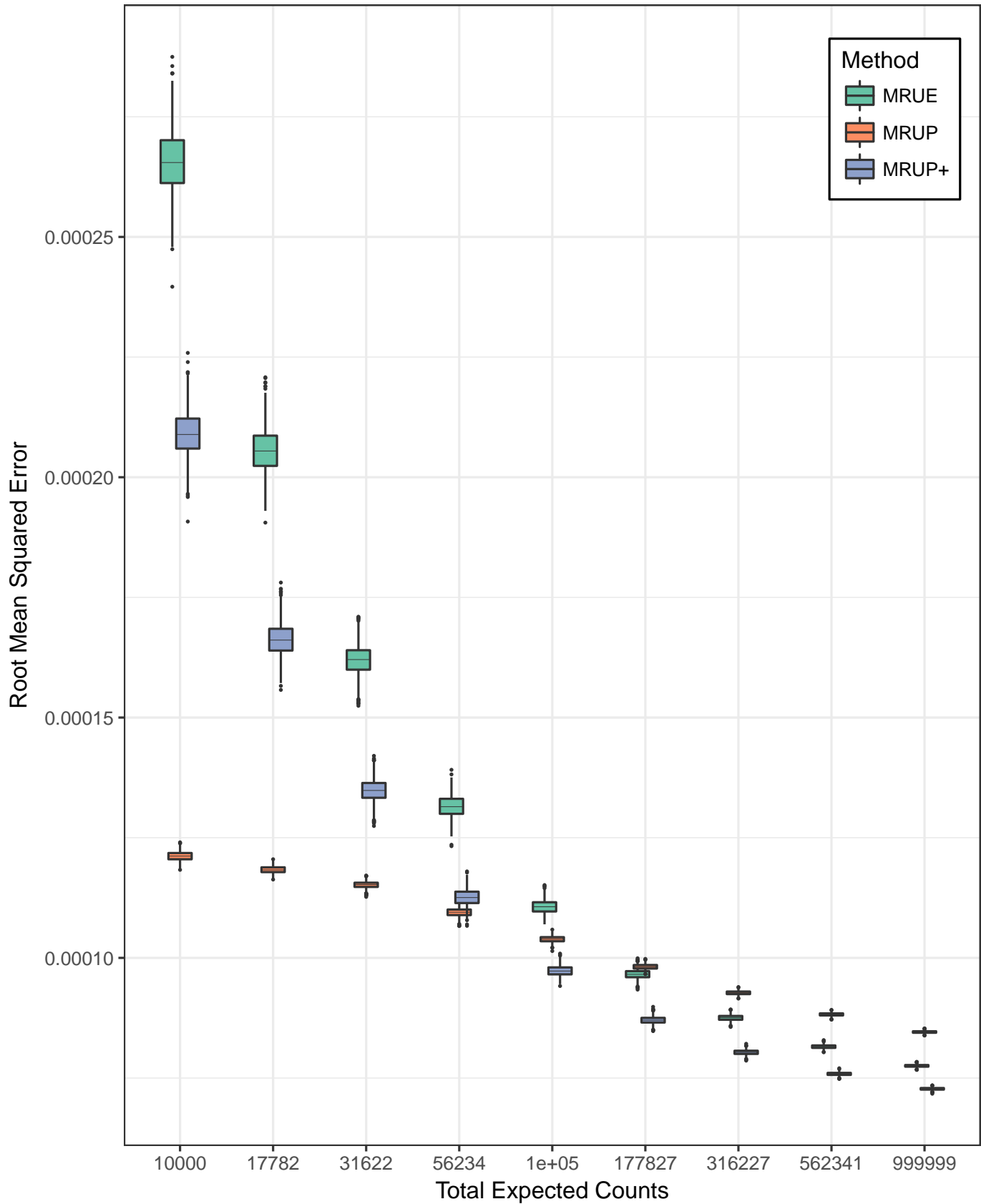


Fig. 5: RMSEs of MRUE, MRUP and MRUP+ reconstructions over 1000 simulations for range of total expected counts.

sets are quite different than the true optimal BPFe parameters. In this paper, we have used the optimization method of [32] to estimate the smoothing parameters using GCVe: an alternative optimization algorithm may be worth exploring. Nevertheless, Figure 4 shows that any of the GCV methods out-performs the MRUE methods, especially at low total expected counts, both in terms of raw RMSE (Figure 5) and relative RMSE efficiency (Figure 6). Indeed, the relative RMSE efficiencies are almost always above 0.95 for the GCV methods. However, the MRU reconstructions are rather poor, especially at lower values of  $\Lambda$ . The MRUP results reported here are a bit more pessimistic than those over limited  $\Lambda$  reported in [16] and [17]. Interestingly and contrary to their results, for larger (but not smaller) values of  $\Lambda$ , MRUE outperforms MRUP: comparison with their computer code indicates that the optimal bandwidths are often attained outside their chosen ranges for several cases. Reducing negative artifacts as per [8] improves MRUE reconstructions slightly – we omit these RMSEs in Figures 5 and 6 for clarity of display. However, the methods of [8] degrades MRUP reconstructions for lower  $\Lambda$ -values: however, with increasing  $\Lambda$ , MRUP+ generally performs the best among all MRUE estimates. The rate of efficiency of reconstructions with increasing  $\Lambda$  obtained using GCV-selected bandwidths is clearly lower than either MRUE or MRUP, but the implications are unclear, given its superior performance at all bandwidths. The results of our simulation study point to the applicability of the GCV method in obtained improved reconstructions with low and high radio-tracer uptake.

### C. Some Theoretical Analysis of the GCV Selector

We close this section with a discussion on some of the theoretical properties of the reconstructions obtained using the GCV-selected bandwidth in an idealized PET setting. We have a realization  $\mathbf{y}$  from an inhomogeneous Poisson Process with mean intensity  $\boldsymbol{\mu} = \mathbf{K}\boldsymbol{\lambda}$ , and  $\Lambda = \sum_{d,\theta} \mu_{d,\theta}$ . Our interest is in estimating  $\mathbf{f} = \boldsymbol{\lambda}/\Lambda$ , for which we propose the estimator  $\hat{\mathbf{f}}^h = \hat{\boldsymbol{\lambda}}^h/\hat{\Lambda}$ . As in [17], we define the loss function in the estimation and prediction domains to be  $L_e(\hat{\mathbf{f}}^h, \mathbf{f}) = \|\hat{\mathbf{f}}^h - \mathbf{f}\|^2$  and  $L_P(\hat{\boldsymbol{\mu}}^h, \boldsymbol{\mu}) = \Lambda^{-2} \|\hat{\boldsymbol{\mu}}^h - \boldsymbol{\mu}\|^2$ , respectively, with corresponding risk functions as  $\mathcal{R}_e(\hat{\mathbf{f}}^h, \mathbf{f})$  and  $\mathcal{R}_P(\hat{\boldsymbol{\mu}}^h, \boldsymbol{\mu})$ . Then, from the SVD of  $\mathbf{K} = \mathbf{U}_1 \mathbf{D}_\bullet \mathbf{V}$ , we get that  $\mathcal{R}_P(\hat{\boldsymbol{\mu}}^h, \boldsymbol{\mu}) = \Lambda^{-2} \text{tr}\{\mathbf{U}_1 \boldsymbol{\Omega}_h^2 \mathbf{U}_1' \boldsymbol{\Sigma} + \boldsymbol{\lambda}' \mathbf{V} \mathbf{D}_\bullet^2 (\mathbf{I}_p - \boldsymbol{\Omega}_h)^2 \mathbf{V}' \boldsymbol{\lambda}\}$ . Let the dispersion matrix of  $\mathbf{y}$  be  $\boldsymbol{\Sigma} \equiv \text{diag}(\boldsymbol{\mu})$  under the idealized conditions of this section. Also

$$\mathcal{R}_e(\hat{\mathbf{f}}^h, \mathbf{f}) = \Lambda^{-2} \text{tr}\{\mathbf{U}_1 \mathbf{D}_\bullet^{-2} \boldsymbol{\Omega}_h^2 \mathbf{U}_1' \boldsymbol{\Sigma} + \boldsymbol{\lambda}' \mathbf{V} (\mathbf{I}_p - \boldsymbol{\Omega}_h)^2 \mathbf{V}' \boldsymbol{\lambda}\} = \Lambda^{-2} \text{tr}\{\mathbf{D}_\bullet^{-2} [\boldsymbol{\Omega}_h^2 \mathbf{U}_1' \boldsymbol{\Sigma} \mathbf{U}_1 + \mathbf{D}_\bullet^2 (\mathbf{I}_p - \boldsymbol{\Omega}_h)^2 \mathbf{V}' \boldsymbol{\lambda} \boldsymbol{\lambda}' \mathbf{V}]\}.$$

Exploiting the diagonality of  $\mathbf{D}_\bullet$  and the nonnegative definiteness of the matrices inside the trace operator yields that  $\mathcal{R}'_e(\hat{\mathbf{f}}^h, \mathbf{f}) \leq \text{tr}\{\mathbf{D}_\bullet^{-2}\} \mathcal{R}'_P(\hat{\boldsymbol{\mu}}^h, \boldsymbol{\mu})$ . Using similar arguments,  $\mathcal{R}'_P(\hat{\boldsymbol{\mu}}^h, \boldsymbol{\mu}) \leq \text{tr}\{\mathbf{D}_\bullet^2\} \mathcal{R}'_e(\hat{\mathbf{f}}^h, \mathbf{f})$  so that both risks are minimized at the same bandwidth. Further, from Theorem 1,

$$\begin{aligned} \Lambda^{-2} \mathbb{E}\zeta(h) &= \Lambda^{-2} \{ \text{tr}[(\mathbf{I}_p - \boldsymbol{\Omega}_h)^2 \mathbf{U}_1' \boldsymbol{\Sigma} \mathbf{U}_1] + \boldsymbol{\lambda}' \mathbf{V} (\mathbf{I}_p - \boldsymbol{\Omega}_h)^2 \mathbf{D}_\bullet^2 \mathbf{V}' \boldsymbol{\lambda} + (1 + c(h))^2 \text{tr} \mathbf{U}_2' \boldsymbol{\Sigma} \mathbf{U}_2 \} \\ &= \mathcal{R}_P(\hat{\boldsymbol{\mu}}^h, \boldsymbol{\mu}) + \Lambda^{-2} \{ (1 + c(h))^2 \text{tr} \boldsymbol{\Sigma} - (2c(h) + c^2(h)) \text{tr} \mathbf{U}_1' \boldsymbol{\Sigma} \mathbf{U}_1 - 2 \text{tr} \boldsymbol{\Omega}_h \mathbf{U}_1' \boldsymbol{\Sigma} \mathbf{U}_1 \} \\ &= \mathcal{R}_P(\hat{\boldsymbol{\mu}}^h, \boldsymbol{\mu}) + \Lambda^{-1} \{ (1 + c(h))^2 \vartheta_{n,p} - (2c(h) + c^2(h)) \text{tr} \boldsymbol{\varphi}_{n,p} - 2 \text{tr} \boldsymbol{\Omega}_h \boldsymbol{\varphi}_{n,p} \}, \end{aligned}$$

where  $\vartheta_{n,p} = \Lambda^{-1} \text{tr} \boldsymbol{\Sigma}$  and the matrix  $\boldsymbol{\varphi}_{n,p} = \Lambda^{-1} \mathbf{U}' \boldsymbol{\Sigma} \mathbf{U}$  are both free of  $\Lambda$ . Thus  $|\mathbb{E}\zeta(h) - \mathcal{R}_P(\hat{\boldsymbol{\mu}}^h, \boldsymbol{\mu})| / \mathcal{R}_P(\hat{\boldsymbol{\mu}}^h, \boldsymbol{\mu}) \rightarrow 0$  as  $\Lambda \rightarrow \infty$ . For  $n \gg p$  as in PET, we have  $\mathbb{E}\zeta'(h) \approx \mathcal{R}'_P(\hat{\boldsymbol{\mu}}^h, \boldsymbol{\mu}) - \frac{2}{\Lambda} \frac{d}{dh} \text{tr} \boldsymbol{\Omega}_h \boldsymbol{\varphi}_{n,p}$  so that for large  $\Lambda$ , the risk has an inflection point close to the bandwidth optimizing  $\mathbb{E}\zeta(h)$ . On the other hand, for smaller values of  $\Lambda$ , the  $h$  optimizing  $\mathcal{R}_P(\hat{\boldsymbol{\mu}}^h, \boldsymbol{\mu})$  is large and close to the minimizer for  $\mathbb{E}\zeta(h)$ . (To see this, consider the example of using a Butterworth filter for which the  $\nu$ th diagonal element of  $\boldsymbol{\Omega}_h$  is  $(1 + h \|\nu\|^r)^{-1}$ .) This discussion provides some theoretical understanding of GCV's good performance in selecting  $h$  for all values of  $\Lambda$  when  $n \gg p$  as is the case with PET or our experiments.

## IV. DISCUSSION

This paper has developed a computationally efficient and practical approach to selecting the filter resolution size in 2D PET reconstructions. The approach uses GCV and outperforms available adaptive methods, irrespective of the total expected rates of emissions. Our approach hinges on the use of implementing FBP through its equivalent BPF form. In general, FBP is far more commonly used than BPF, but this is arguably on grounds of its roots in X-ray computed tomography where reconstruction can begin along LORs for a given projection angle even while data along other projection angles are being acquired. In emission tomography, this is not possible because the data need to be completely acquired in the given time interval before reconstruction can begin. The suggested approach also has the ability to incorporate a wider class of 2D reconstruction filters with the potential for further improving reconstruction performance.

The methodology presented here focused on BPF reconstructions. Extensions of the approach could make possible the practical implementation of penalized reconstruction methods in PET such as in [27] or for regularizing reconstructions obtained using [5]–[7]. These extensions would require further development before they can be adopted for routine clinical use. Thus, we see that while the methods developed in this paper show promise in improving 2D PET reconstruction, many issues remain that merit further attention.

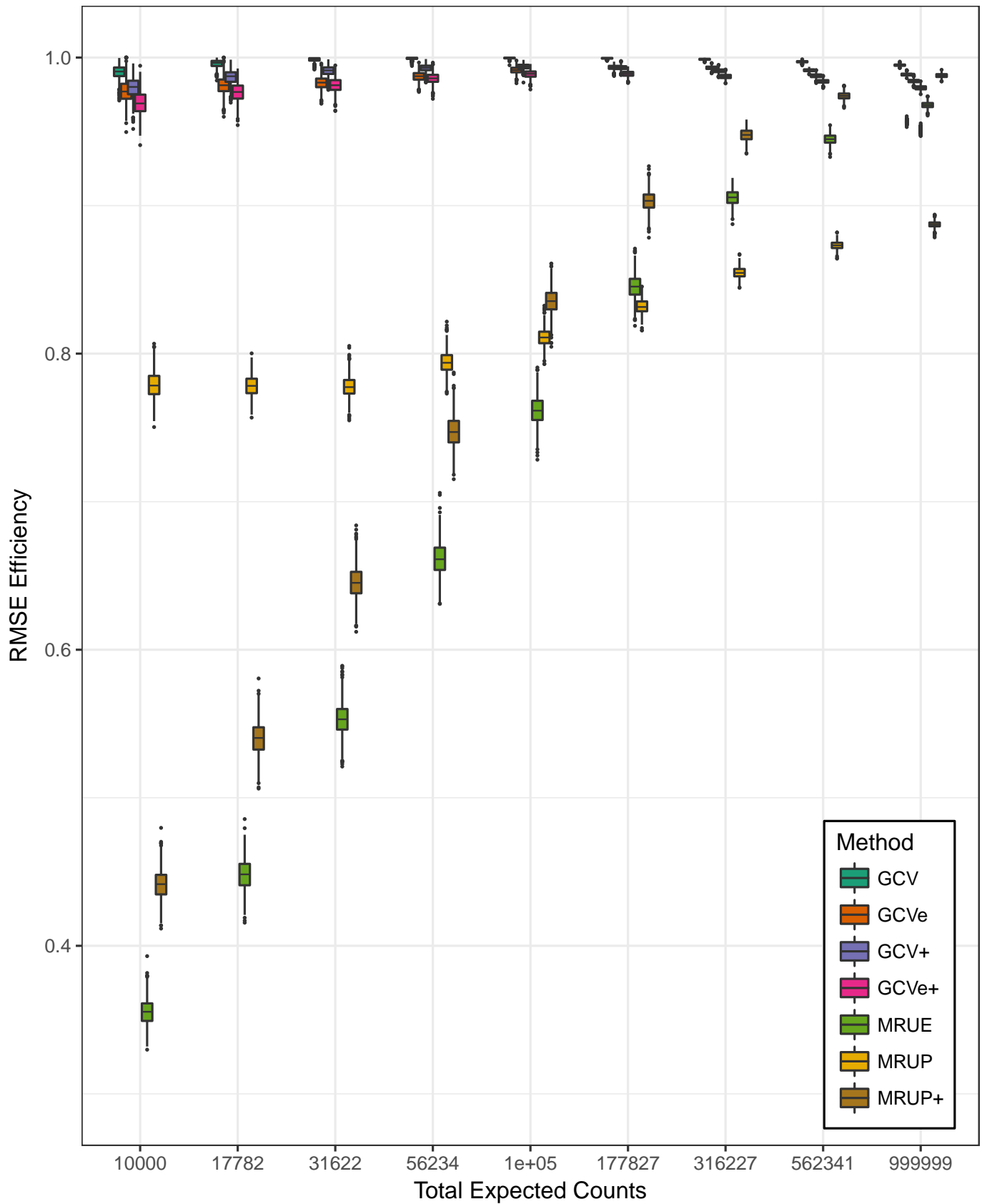


Fig. 6: RMSE of reconstructions relative to the corresponding gold standard for different total expected counts using the different bandwidth selection and reconstruction methods.

## APPENDIX

### A. Proof of Theorem 1

The development and proof of the theorem closely mirror that of estimating the ridge regression parameter in [20]. The LOOCV mean squared error (CVMSE) is  $\tau(h) = \frac{1}{n} \sum_{j=1}^n (\mathbf{k}'_j \hat{\lambda}_{-j}^h - y_j)^2$ . Using the Sherman-Morrison-Woodbury theorem and denoting the (unsmoothed) LS reconstruction by  $\hat{\lambda} = \mathbf{Q}_K \mathbf{K}' \mathbf{y}$ , where  $\mathbf{Q}_K \equiv (\mathbf{K}' \mathbf{K})^{-1}$  in order to compress expressions, it follows that

$$\mathbf{k}'_j \hat{\lambda}_{-j}^h - y_j = \mathbf{k}'_j \mathbf{S}_h \left[ \mathbf{Q}_K + \frac{\mathbf{Q}_K \mathbf{k}_j \mathbf{k}'_j \mathbf{Q}_K}{1 - \mathbf{k}'_j \mathbf{Q}_K \mathbf{k}_j} \right] (\mathbf{K}' \mathbf{y} - \mathbf{k}_j y_j) - y_j = (\mathbf{k}'_j \hat{\lambda}^h - y_j) + \frac{\Gamma_{jj,h}}{1 - \Gamma_{jj}} (\mathbf{k}'_j \hat{\lambda} - y_j)$$

where  $\Gamma_{jj,h} = \mathbf{k}'_j \mathbf{S}_h \mathbf{Q}_K \mathbf{k}_j$  and  $\Gamma_{jj} = \mathbf{k}'_j \mathbf{Q}_K \mathbf{k}_j$ . Let  $\Delta_h$  be the diagonal matrix with  $\Gamma_{jj,h}/(1 - \Gamma_{jj})$  as the  $(j,j)$ th element. Then, using the above, the CVMSE reduces to

$$\begin{aligned} \tau(h) &= \frac{1}{n} \left\{ \mathbf{y}' [\mathbf{I}_n - \mathbf{K} \mathbf{S}_h \mathbf{Q}_K \mathbf{K}']' [\mathbf{I}_n - \mathbf{K} \mathbf{S}_h \mathbf{Q}_K \mathbf{K}'] \mathbf{y} \right. \\ &\quad + 2\mathbf{y}' [\mathbf{I}_n - \mathbf{K} \mathbf{S}_h \mathbf{Q}_K \mathbf{K}']' \Delta_h [\mathbf{I}_n - \mathbf{K} \mathbf{Q}_K \mathbf{K}'] \mathbf{y} \\ &\quad \left. + \mathbf{y}' [\mathbf{I}_n - \mathbf{K} \mathbf{Q}_K \mathbf{K}']' \Delta_h^2 [\mathbf{I}_n - \mathbf{K} \mathbf{Q}_K \mathbf{K}'] \mathbf{y} \right\}. \end{aligned} \quad (7)$$

Let  $\mathbf{D}_\bullet$  be the diagonal matrix of the square root of the  $p$  eigenvalues of  $\mathbf{K}' \mathbf{K}$ . Let  $\mathbf{K} = \mathbf{U} \mathbf{D} \mathbf{V}'$  be the SVD of  $\mathbf{K}$  with  $\mathbf{U}$  as in the theorem statement,  $\mathbf{D}$  be  $\mathbf{D}_\bullet$  augmented row-wise by an  $(n-p) \times p$  matrix of zeros, and  $\mathbf{V}$  have columns containing the right singular vectors of  $\mathbf{K}$ . Further, let  $\mathbf{W}$  be the corresponding unitary matrix which diagonalizes a 1D (see [31]) or 2D (see Theorem 5) circulant matrix. Under the rotated generalized linear model having observations  $\tilde{\mathbf{y}} = \mathbf{W} \mathbf{U}' \mathbf{y}$ , the reconstruction problem reformulates to estimating  $\lambda$  from  $\mathbf{E}(\tilde{\mathbf{y}}) = \mathbf{W} \mathbf{D} \mathbf{V}' \lambda \equiv \tilde{\mathbf{K}} \lambda$ , where  $\tilde{\mathbf{K}} = \mathbf{W} \mathbf{D} \mathbf{V}'$ .

Now  $\tilde{\mathbf{K}}' \tilde{\mathbf{K}} = \mathbf{V} \mathbf{D}_\bullet^2 \mathbf{V}'$  so that  $\tilde{\mathbf{K}}(\tilde{\mathbf{K}}' \tilde{\mathbf{K}})^{-1} \tilde{\mathbf{K}}'$  and  $\tilde{\mathbf{K}} \mathbf{S}_h(\tilde{\mathbf{K}}' \tilde{\mathbf{K}})^{-1} \tilde{\mathbf{K}}'$  are both circulant, with each having exactly  $p$  positive and non-zero eigenvalues given by the diagonal elements of  $\mathbf{I}_p$  and  $\Omega_h$  respectively. Consequently  $(\mathbf{I}_n - \tilde{\mathbf{K}}(\tilde{\mathbf{K}}' \tilde{\mathbf{K}})^{-1} \tilde{\mathbf{K}}') = \mathbf{W} \mathcal{D}_{(\mathbf{0}_p, \mathbf{I}_{n-p})} \mathbf{W}^*$  and  $(\mathbf{I}_n - \tilde{\mathbf{K}} \mathbf{S}_h(\tilde{\mathbf{K}}' \tilde{\mathbf{K}})^{-1} \tilde{\mathbf{K}}') = \mathbf{W} \mathcal{D}_{(\mathbf{I}_p - \Omega_h, \mathbf{I}_{n-p})} \mathbf{W}^*$  where  $\mathbf{W}^*$  is the complex conjugate transpose of  $\mathbf{W}$ ,  $\mathbf{0}_p$  is a  $p \times p$  matrix of zeros and  $\mathcal{D}_{(\cdot, \cdot)}$  denotes a block-diagonal matrix. Therefore, both  $\tilde{\mathbf{K}} \mathbf{S}_h(\tilde{\mathbf{K}}' \tilde{\mathbf{K}})^{-1} \tilde{\mathbf{K}}'$  and  $(\mathbf{I} - \tilde{\mathbf{K}}(\tilde{\mathbf{K}}' \tilde{\mathbf{K}})^{-1} \tilde{\mathbf{K}}')$  are circulant (the latter is also idempotent) with constant diagonals. In the rotated framework,  $\Gamma_{jj,h} = \text{tr}(\Omega_h)/n$  (note that  $\text{tr}(\Omega_h)$  is  $p$  times any diagonal element of  $\mathbf{S}_h$ ) while  $1 - \Gamma_{jj} = (n-p)/n$ , and so  $\Delta_h = c(h) \mathbf{I}_n$ . In the rotated framework, we consider the three terms in (7) individually. The first term  $\tilde{\mathbf{y}}' [\mathbf{I} - \tilde{\mathbf{K}} \mathbf{S}_h(\tilde{\mathbf{K}}' \tilde{\mathbf{K}})^{-1} \tilde{\mathbf{K}}'] [\mathbf{I} - \tilde{\mathbf{K}} \mathbf{S}_h(\tilde{\mathbf{K}}' \tilde{\mathbf{K}})^{-1} \tilde{\mathbf{K}}'] \tilde{\mathbf{y}}$  reduces to  $\mathbf{y}' \mathbf{U} \mathcal{D}_{(\mathbf{I}_p - \Omega_h, \mathbf{I}_{n-p})}^2 \mathbf{U}' \mathbf{y} = z'_1 (\mathbf{I}_p - \Omega_h)^2 z_1 + z'_2 z_2$ , while the second term  $2\tilde{\mathbf{y}}' [\mathbf{I}_n - \tilde{\mathbf{K}} \mathbf{S}_h(\tilde{\mathbf{K}}' \tilde{\mathbf{K}})^{-1} \tilde{\mathbf{K}}']' \Delta_h [\mathbf{I}_n - \tilde{\mathbf{K}}(\tilde{\mathbf{K}}' \tilde{\mathbf{K}})^{-1} \tilde{\mathbf{K}}'] \tilde{\mathbf{y}} \equiv 2c(h) \mathbf{y}' \mathbf{U} \mathcal{D}_{(\mathbf{I}_p - \Omega_h, \mathbf{I}_{n-p})} \mathcal{D}_{(\mathbf{0}_p, \mathbf{I}_{n-p})} \mathbf{U} \mathbf{y} = 2c(h) z'_1 z_2$ . The third term  $\tilde{\mathbf{y}}' [\mathbf{I}_n - \tilde{\mathbf{K}}(\tilde{\mathbf{K}}' \tilde{\mathbf{K}})^{-1} \tilde{\mathbf{K}}']' \Delta_h^2 [\mathbf{I}_n - \tilde{\mathbf{K}}(\tilde{\mathbf{K}}' \tilde{\mathbf{K}})^{-1} \tilde{\mathbf{K}}'] \tilde{\mathbf{y}} \equiv c^2(h) \mathbf{y}' \mathbf{U} \mathcal{D}_{(\mathbf{0}_p, \mathbf{I}_{n-p})} \mathbf{U}' \mathbf{y} = c^2(h) z'_2 z_2$ . Theorem 1 follows, after scaling all sides by  $n$ .  $\square$

### B. Proof of Theorem 2

Let  $\ell = (p+1)/2$  if  $p$  is odd or  $\ell = p/2$  if  $p$  is even. Let  $\mathbf{c} = \{c_0, c_1, c_2, \dots, c_{\ell-1}, c_\ell, c_{\ell-1}, \dots, c_2, c_1\}$  be the first row of  $\mathbf{C}$  for even  $p$ ; the middle term  $c_\ell$  is absent for odd  $p$ . Writing the  $k$ th of the  $p$  complex roots of unity as  $\exp\{i2\pi k/p\} = \cos(2\pi k/p) + i \sin(2\pi k/p)$ , the  $k$ th eigenvalue of  $\mathbf{C}$  is  $d_k = \sum_{j=0}^{p-1} c_j \omega_k^j = c_0 + \sum_{j=1}^{\ell-1} c_j \cos(2\pi k j/p) + c_{p/2} (-1)^\ell; 0 \leq k \leq p-1$ , with the last term in the summation absent for  $p$  odd. From [31] or directly, an eigenvector corresponding to  $d_k$  is  $\gamma(\omega_k) = \{1, \omega_k^1, \omega_k^2, \dots, \omega_k^{p-1}\}$ . Further,  $d_k = d_{p-k}$  for  $k = 1, 2, \dots, \ell-1$ . This means that any symmetric circulant matrix has two (only one for  $p$  odd) real eigenvalues of algebraic multiplicity one with eigenvectors given, up to constant division, by  $\mathbf{1} = \{1, 1, \dots, 1\}$  and (for  $p$  even)  $\pm\mathbf{1} = \{1, -1, 1, -1, \dots, 1, -1\}$ . There are at most  $\ell-1$  distinct eigenvalues of algebraic multiplicity 2: for  $1 \leq k \leq \ell-1$ , the eigenvectors corresponding to  $d_k$  are  $\gamma(\omega_k)$  and  $\gamma(\bar{\omega}_k)$ , where  $\bar{\omega}_k$  is the complex conjugate of  $\omega_k$ . Therefore,  $\gamma(\omega_k) + \gamma(\bar{\omega}_k)$  and  $i(\gamma(\omega_k) - \gamma(\bar{\omega}_k))$  are also distinct (and real) eigenvectors that correspond to  $d_k$ . Theorem 2 follows.  $\square$

## REFERENCES

- [1] M. Ter-Pogossian, M. E. Raichle, and B. E. Sobel, "Positron emission tomography," *Scientific American*, vol. 243(4), pp. 170–181, 1980.
- [2] D. Hawe, F. R. H. Fernández, L. O'Suilleabháin, J. Huang, E. Wolsztynski, and F. O'Sullivan, "Kinetic analysis of dynamic positron emission tomography data using open-source image processing and statistical inference tools," in *Wiley Interdisciplinary Reviews: Computational Statistics*, 2012, vol. 4, no. 3, pp. 316–322.
- [3] F. O'Sullivan, "Locally constrained mixture representation of dynamic imaging data from pet and mr studies," *Biostatistics*, vol. 7:2, pp. 318–338, 2006.
- [4] E. Wolsztynski, F. O'Sullivan, J. O'Sullivan, and J. F. Eary, "Statistical assessment of treatment response in a cancer patient based on pre-therapy and post-therapy FDG-PET scans," *Statistics in Medicine*, vol. 36, no. 7, pp. 1172–1200, 2017.
- [5] Y. Vardi, L. A. Shepp, and L. A. Kaufman, "Statistical model for positron emission tomography," *Journal of the American Statistical Association*, vol. 80, pp. 8–37, 1985.

- [6] P. J. Green, "Bayesian reconstruction from positron emission tomography using a modified EM algorithm," *IEEE Transactions on Medical Imaging*, vol. 9, pp. 84–93, 1990.
- [7] F. O'Sullivan and L. O'Suilleabháin, "A multi-grid approach to ML reconstruction in PET: A fast alternative to EM-based techniques," in *2013 IEEE Nuclear Science Symposium and Medical Imaging Conference Record*, 2013, pp. 1–5.
- [8] F. O'Sullivan, Y. Pawitan, and D. Haynor, "Reducing negativity artifacts in emission tomography: Post-processing filtered backprojection solutions," *IEEE Transactions on Medical Imaging*, vol. 12, pp. 653–663, 1993.
- [9] F. O'Sullivan, "A study of least squares and maximum likelihood for image reconstruction in positron emission tomography," *Annals of Statistics*, vol. 23:4, pp. 1267–1300, 1995.
- [10] P. Hall, "On global properties of variable bandwidth density estimators," *Annals of Statistics*, vol. 20, pp. 762–778, 1992.
- [11] D. Nychka and D. D. Cox, "Convergence rates for regularized solutions of integral equations from discrete noisy data," *Annals of Statistics*, vol. 17, pp. 556–572, 1989.
- [12] B. W. Silverman, *Density Estimation for Statistics and Data Analysis*. London: Chapman and Hall, 1986.
- [13] C. J. Stone, "An asymptotically optimal window selection rule for kernel density estimates," *Annals of Statistics*, vol. 12, pp. 1289–1297, 1984.
- [14] G. Wahba, *Spline Models in Statistics*. Philadelphia: SIAM, 1990.
- [15] D. A. Girard, "Optimal regularized reconstruction in computer tomography," *SIAM Journal of Scientific and Statistical Computation*, vol. 8, pp. 934–950, 1987.
- [16] Y. Pawitan and F. O'Sullivan, "Data-dependent bandwidth selection for emission computed tomography reconstruction," *IEEE Transactions on Medical Imaging*, vol. 12, pp. 653–663, 1993.
- [17] F. O'Sullivan and Y. Pawitan, "Bandwidth selection for indirect density estimation based on corrupted histogram data," *Journal of the American Statistical Association*, vol. 91, pp. 610–627, 1996.
- [18] S. Geisser, "The predictive sample reuse method with applications," *Journal of the American Statistical Association*, vol. 70(350), pp. 320–328, 1975.
- [19] C. J. Stone, "Cross-validation and multinomial prediction," *Biometrika*, vol. 61, pp. 509–515, 1974.
- [20] G. H. Golub, M. Heath, and G. Wahba, "Generalized crossvalidation as a method for choosing a good ridge parameter," *Technometrics*, vol. 21, pp. 215–223, 1979.
- [21] P. Craven and G. Wahba, "Smoothing noisy data with spline functions," *Numerical Methods*, vol. 31, pp. 377–403, 1979.
- [22] S. J. Reeves and R. M. Merserau, "Optimal estimation of the regularization parameter and stabilizing functional for regularized image restoration," *Optical Engineering*, vol. 29(5), pp. 445–454, 1990.
- [23] S. J. Reeves, "A cross-validation framework for solving image restoration problems," *Journal of Visual Communications and Image Representation*, vol. 3, pp. 433–445, 1992.
- [24] N. Nguyen, P. Milanfar, and G. Golub, "Efficient generalized cross-validation with applications to parametric image restoration and resolution enhancement," *IEEE Transactions on Image Processing*, vol. 10(9), pp. 1299–1308, 2001.
- [25] P. Hall and D. M. Titterington, "Common structure of techniques for choosing smoothing parameters in regression problems," *Journal of the Royal Statistical Society, B*, vol. 49, pp. 184–198, 1987.
- [26] A. M. Thompson, J. C. Brown, J. W. Kay, and D. M. Titterington, "A study of methods of choosing the smoothing parameter in image restoration by regularization," *IEEE Transactions on Pattern Analysis and Machine Intelligence*, vol. 13(4), pp. 326–339, 1991.
- [27] A. M. Thompson, J. W. Kay, and D. M. Titterington, "A cautionary note about crossvalidatory choice," *Journal of Statistical Computing and Simulation*, vol. 33, pp. 199–216, 1989.
- [28] F. Natterer, *Mathematics of Computerized Tomography*. New York: Wiley, 1986.
- [29] M. Wand and M. Jones, *Kernel Smoothing*. London: Chapman and Hall, 1995.
- [30] J. W. Demmel, *Applied Numerical Linear Algebra*. Philadelphia: SIAM, 1997.
- [31] R. Bellman, *An Introduction to Matrix Analysis*. New York: McGraw-Hill, 1960.
- [32] J. A. Nelder and R. Mead, "A simplex algorithm for function minimization," *Computer Journal*, vol. 7, pp. 308–313, 1965.
- [33] E. J. Hoffman, P. D. Cutler, W. M. Digby, and J. C. Mazziotta, "3-d phantom to simulate cerebral blood flow and metabolic images for pet," *IEEE Transactions on Nuclear Science*, vol. 37, pp. 616–620, 1990.
- [34] M. E. Phelps, S. C. Huang, E. J. Hoffman, C. Selin, L. Sokoloff, and D. E. Kuhl, "Tomographic measurement of local cerebral glucose metabolic rate in humans with [<sup>18</sup>F]-2-fluoro-2-deoxy-d-glucose: Validation of method," *Annals of Neurology*, vol. 6, pp. 371–388, 1979.